nanomanufacturing

MDPI

Article

Bio-Inspired Hierarchical Carbon Structures Coated with Zeolite for High-Yield Carbon Nanotube Synthesis

Kamrun Nahar Fatema [1], Md Rokon Ud Dowla Biswas [2], Se Young Kim [3], In Sub Han [3], Young Suk Kim [4], Sung Chil Lee [4] and Ik Jin Kim [2,4,*]

[1] School of Mechanical Engineering, Chonnam National University, Gwangju 61186, Republic of Korea
[2] Research & Development Center, HanTech Co., Ltd., Anyang-si 15809, Republic of Korea
[3] Korea Institute of Energy Research, High Temperature Electrolysis Lab., Yuseung-gu, Daejeon City 34129, Republic of Korea
[4] German Mongolian Institute for Resources and Technology, Ulaanbaatar 12600, Mongolia
* Correspondence: ikjin@gmit.edu.mn

Abstract

Efficient synthesis of carbon nanotubes (CNTs) remains challenging due to catalyst nanoparticle agglomeration during catalytic chemical vapor deposition (CCVD). In this study, biomorphic carbon materials (BCMs) derived from natural wood were coated with LTA zeolite and used as structured supports for cobalt-catalyzed CNT synthesis. The carbonized BCMs preserved their hierarchical cellular architecture, while the LTA zeolite coating provided a microporous interfacial layer for cobalt catalyst loading. CNTs were synthesized by CCVD using acetylene at 650 °C. CNT growth was successfully achieved on the LTA-zeolite-coated biomorphic supports, with TGA-derived carbon deposition values ranging from 2.21% to 21.82%. Red pine and red cedar exhibited comparatively low carbon deposition values of 2.40% and 2.21%, respectively, whereas cypress and Gorman spruce showed substantially higher values of 21.82% and 21.01%, respectively. The highest carbon deposition value was obtained for the cypress-derived BCM. Transmission electron microscopy confirmed the formation of well-developed multiwalled carbon nanotubes with support-dependent diameters and highly graphitized walls. The results demonstrate successful CNT growth on LTA-zeolite-coated biomorphic carbon supports and reveal pronounced support-dependent differences associated with the biomorphic pore architecture and gas-transport characteristics.

Keywords: biomorphic carbon material; carbon nanotube; catalytic chemical vapor deposition; LTA zeolite; permeability

Check for updates

Academic Editor: Sergei A. Kulinich

Received: 10 August 2026
Revised: 20 October 2026
Accepted: 26 October 2026
Published: 2 November 2026

Copyright: © 2026 by the authors. Licensee MDPI, Basel, Switzerland. This article is an open access article distributed under the terms and conditions of the Creative Commons Attribution (CC BY) license.

1. Introduction

Carbon nanotubes (CNTs) have attracted sustained interest because of their high surface area, large aspect ratio, and distinctive structural, electrical, and physicochemical properties. Owing to these features, CNT-based materials have been investigated for a broad range of applications, including adsorption, catalysis, energy storage, sensing, and membrane-related systems [1–4]. In porous architectures, CNT incorporation is particularly attractive because it can provide interconnected pathways for mass transport while preserving the functional characteristics of graphitic nanocarbons.

CNTs are generally synthesized through the catalytic decomposition of hydrocarbon gases, such as methane and acetylene, over transition-metal catalysts including Fe, Co, and Ni [5,6]. However, uniform and efficient CNT growth remains difficult to achieve because

catalyst nanoparticles tend to agglomerate at elevated temperature. Such agglomeration reduces the number of active sites, broadens the CNT diameter distribution, and lowers the overall growth efficiency [7].

Various porous templates and catalyst supports, including alumina, mesoporous silica, and zeolites, have been employed for CNT synthesis [8–12]. LTA zeolite is of interest as a catalyst-support material because of its well-defined microporous structure and its capacity to host metal species [11,12].

Biomorphic carbon materials (BCMs) derived from natural wood provide an additional advantage as structured carbon supports. After carbonization, wood preserves its intrinsic cellular architecture, resulting in an anisotropic yet interconnected porous carbon framework [5,13–15]. This hierarchical pore network can facilitate precursor-gas transport and provide a three-dimensional scaffold for catalyst deposition and CNT growth. Because the pore morphology varies with wood species, the resulting BCMs may exhibit different permeability and transport characteristics, which can, in turn, influence CNT formation during CCVD.

In this study, LTA-zeolite-coated biomorphic carbon supports derived from red pine, red cedar, cypress, and Gorman spruce were used for cobalt-catalyzed CNT synthesis by CCVD. The effects of the wood-derived hierarchical pore architecture on CNT morphology, carbon deposition, and gas-permeability characteristics were comparatively evaluated under the same catalyst-loading and CCVD conditions. The synthesized composites were characterized by field-emission scanning electron microscopy (FESEM), transmission electron microscopy (TEM), Raman spectroscopy, thermogravimetric analysis (TGA), and gas permeability measurements, while the phase identity of the LTA-zeolite coating was supported by previously reported XRD characterization [16].

2. Experimental

2.1. Raw Materials

Tetramethylammonium hydroxide (TMAOH, Sigma-Aldrich, St. Louis, MO, USA), aluminum isopropoxide (AIP, Sigma-Aldrich, St. Louis, MO, USA), tetraethyl orthosilicate (TEOS, Sigma-Aldrich, St. Louis, MO, USA), and sodium hydroxide (NaOH, Sigma-Aldrich, St. Louis, MO, USA) were used for the synthesis and coating of the LTA zeolite template on the BCMs. Cobalt (II) chloride hexahydrate (CoCl2 • 6H2O, ≥97.0%, SAMCHUN Pure Chemical Co., Ltd., Pyeongtaek-si, Republic of Korea) was used as the cobalt precursor for catalyst loading. Ethanol (Daejung Chemicals & Metals Co., Ltd., Siheung-si, Republic of Korea) was used for washing the samples after cobalt impregnation. Nitrogen (N_2, Messer Korea Co., Ltd., Ansan-si, Republic of Korea) was used as the inert gas during carbonization and thermal treatment and as the process gas during CCVD. Acetylene (C_2H_2, SAMJUNG GAS Co. LTD, Incheon, Republic of Korea) was used as the carbon source for CNT growth at a flow rate of 10 sccm. Carbon nanotubes were grown by the CCVD method at 650 °C for 60 min.

2.2. Preparation of Biomorphic Carbon Materials

Natural wood precursors, including red pine, red cedar, cypress, and Gorman spruce, were used to prepare biomorphic carbon materials. The specimens were carbonized under flowing N_2 to preserve their intrinsic cellular structures. Samples were heated at 0.5 °C min^{-1} to 600 °C under an N_2 flow of 10 cm^3 min^{-1} for 6–8 h, followed by heating to 1000 °C at 3 °C min^{-1}. During pyrolysis, the lignocellulosic components gradually decomposed and volatile species were removed, resulting in a carbon-rich framework that retained the natural cellular morphology as a biomorphic porous structure (Figure 1).

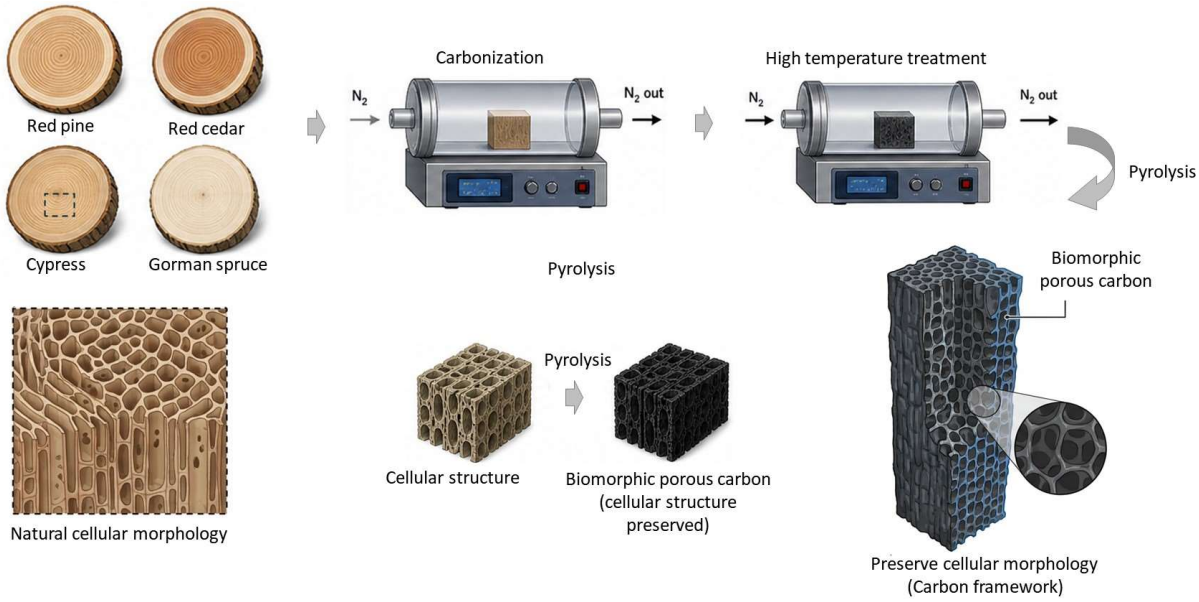


Figure 1. Schematic illustration of the carbonization of natural wood to form biomorphic carbon materials (BCMs).

2.3. Synthesis of LTA-Zeolite-Coated BCMs and CNT Growth

To synthesize the LTA zeolite coating on the BCMs, the mother solution was prepared at a molar ratio of AIP: TEOS: TMAOH: NaOH: H_2O = 1:2.2:2.4:0.3:200 [15]. For LTA coating, 20.8 g of AIP was dissolved in 280 g of distilled water and stirred for 2 h, after which 87.0 g of TMAOH was added. Separately, 1.0 g of NaOH was dissolved in 80.0 g of distilled water, followed by the dropwise addition of 46.0 g of TEOS. The two solutions were then mixed and stirred until the mother solution became clear, and the solution was transferred to a Teflon-lined container containing the BCM specimens. After aging overnight at room temperature, the sealed container was placed in an autoclave and maintained at 90 °C for 3 days for hydrothermal synthesis of the zeolite coating. The phase identity of the hydrothermally synthesized LTA coating prior to CCVD was previously verified by XRD in our earlier study (see i Ref. [16]). After zeolite coating, cobalt catalyst species were introduced onto the LTA-coated BCMs by a wet impregnation/ion-exchange process. The zeolite-coated BCMs were placed on a stainless-steel mesh in a beaker containing 250 mL of an aqueous $CoCl_2{\cdot}6H_2O$ solution. Accordingly, the cobalt loading condition is reported in terms of the nominal precursor amount used for impregnation (1.2 mmol $CoCl_2{\cdot}6H_2O$ in 250 mL, corresponding to 4.8 mM). The samples were stirred at room temperature for 24 h, washed with ethanol, and dried in a forced-convection oven at 323 K for 24 h. The dried catalyst-loaded supports were subsequently calcined at 450 °C under N_2. The same nominal cobalt precursor amount, precursor concentration, and catalyst-loading procedure were applied to all wood-derived BCM supports to maintain consistent catalyst-preparation conditions. Before acetylene exposure, the catalyst-loaded supports were heated under N_2 to 300 °C over 60 min and maintained at this temperature for approximately 30 min. The temperature was then increased to 650 °C over 80 min, followed by a 15 min stabilization period at 650 °C under N_2. Acetylene was subsequently introduced, and CNT growth was carried out at 650 °C for 60 min. No separate H_2 reduction step was described in the original preparation procedure. The overall catalyst-loading and CNT-growth procedure is summarized schematically in Figure 2.

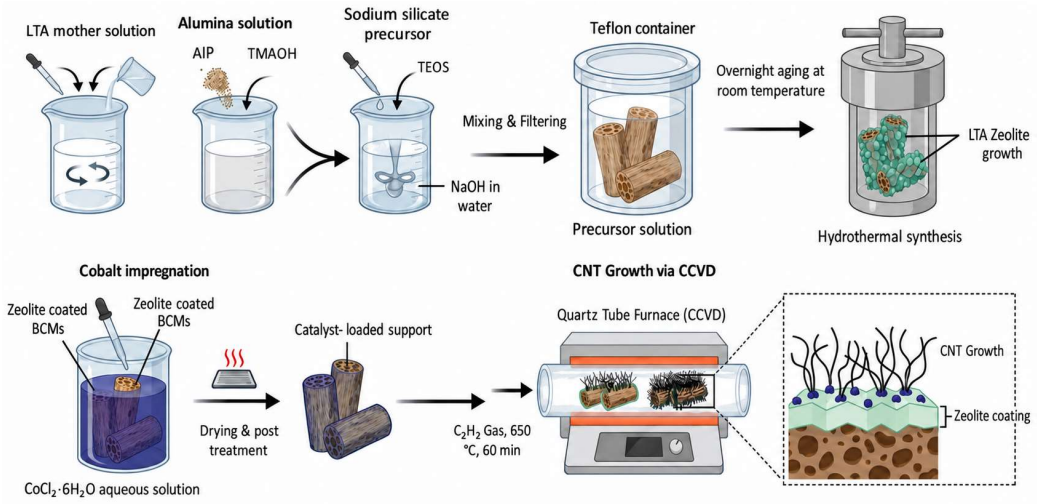


Figure 2. Schematic illustration of the hydrothermal synthesis and coating of LTA zeolite on the BCM surface and growth of CNTs on Co-loaded LTA-zeolite-coated BCMs by CCVD.

2.4. Characterization

The morphology of the BCMs, LTA-zeolite-coated BCMs, and CNT-grown composites was examined using field-emission scanning electron microscopy (FESEM, LEO 1530 VP, LEO Elektronenmikroskopie GmbH, Oberkochen, Germany) operated at an acceleration voltage of 1.0 kV. Transmission electron microscopy (TEM, JEOL JEM-3011, JEOL Ltd., Tokyo, Japan) operated at 200 kV was used to observe CNT morphology and wall structure. Phase identification of the zeolite-coated BCMs was previously carried out by powder X-ray diffraction (XRD, Rigaku D/max 2500 VL/PC, Rigaku Corporation, Tokyo, Japan) using Cu Kα radiation ($\lambda = 1.5418$ Å) at 40 kV and 40 mA, as reported in our earlier study [16]. Diffraction patterns were collected over a 2θ range of 10–70°. Raman spectroscopy (FRA-106/S, Bruker Optik, Ettlingen, Germany) with a 1064 nm Nd: YAG laser was employed to assess graphitic ordering and defect-related characteristics through the D and G bands. The Raman ratios, TGA-derived carbon deposition values, and permeability results are reported as individual experimental values because replicate datasets sufficient for statistical analysis were not available. Accordingly, standard deviations and error bars are not reported, which represents a limitation of the present study.

2.5. Permeability Analysis

Gas permeability was evaluated using a custom-built apparatus based on Darcy's law. The device consisted of a steel frame, polyurethane tubing with a diameter of 6 mm for nitrogen inlet and outlet, one-touch fittings for sample mounting, pressure gauges for measuring upstream and downstream pressures, and a bubble flow meter for determining the gas flow rate. Each sample was mounted in a polymethyl methacrylate (PMMA) cuvette, sealed with Teflon tape to prevent gas leakage, and fixed using epoxy adhesive as shown in Figure 3.

The permeability of the CNT-grown, zeolite-coated BCMs was calculated using Darcy's law:

$$Q = -\frac{\kappa A}{\mu}\frac{\left(P_{dw} - P_{up}\right)}{L}$$

where Q is the volumetric gas flow rate ($m^3\ s^{-1}$), κ is the permeability (m^2), A is the sample cross-sectional area (m^2), μ is the gas viscosity (Pa·s), P_{up} and P_{dw} are the upstream and downstream pressures (Pa), respectively, and L is the sample length (m).

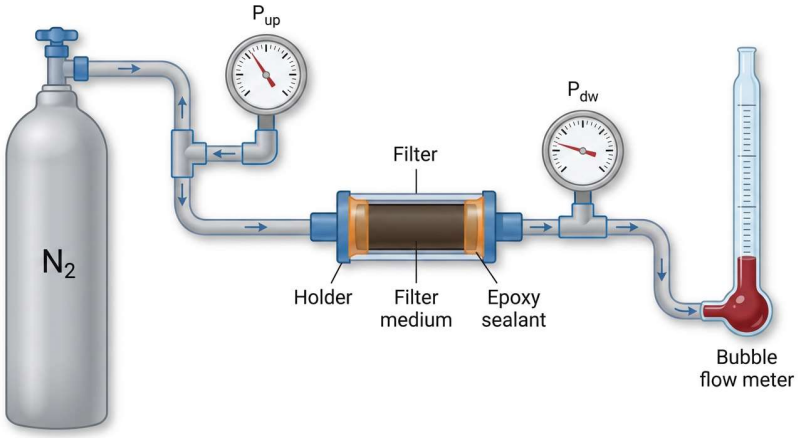


Figure 3. Schematic diagram of the custom-built permeability measurement apparatus used for evaluating gas transport through the CNT-grown, LTA-zeolite-coated BCM samples.

3. Results and Discussion

3.1. Structural Evolution of Biomorphic Carbon Materials

During pyrolysis, the wood precursors underwent devolatilization and decomposition of hemicellulose, cellulose, and lignin, producing carbon-rich chars while preserving their original anatomical structure [14]. Our previous study showed that the XRD patterns of biomorphic carbon materials (BCMs) derived from red pine, red cedar, cypress, and Gorman spruce exhibited broad peaks at approximately 24° and 43° (2θ), corresponding to the (002) and (100) planes of turbostratic graphitic carbon [14]. The broad diffraction peaks indicate disordered graphene-like layers with limited long-range order. Similar diffraction patterns among all BCMs suggest comparable carbonization, with minor differences attributed to variations in wood composition and pore development. These results confirm the formation of porous graphitic carbon frameworks that retained the biomorphic structure and served as suitable supports for zeolite coating and catalyst loading. The crystalline phase of the hydrothermally synthesized zeolite coating was previously characterized by XRD before CNT growth [16]. The LTA-coated BCM exhibited characteristic reflections at approximately 2θ = 10° (220) and 24° (600), consistent with the LTA reference pattern (JCPDS No. 97-002-4901). The previous XRD analysis identified the coating as a single LTA phase, confirming that the zeolite used in the present study corresponds to LTA rather than an MFI-type phase.

3.2. Morphology and Pore Architecture of BCMs

FESEM images (Figure 4) confirmed that the intrinsic cellular architecture of the wood was preserved after carbonization, producing honeycomb-like porous carbon scaffolds with aligned channels and interconnected voids. Although all biomorphic carbon materials (BCMs) retained similar porous networks, pore morphology varied with wood species. Red pine exhibited relatively open pores (28–39 μm), red cedar showed denser structures with smaller pores (21–38 μm), cypress displayed a more uniform pore arrangement, and Gorman spruce had highly symmetrical, open cellular features. These structural differences can influence gas transport, diffusion, and catalyst accessibility during CCVD. The preserved macroporous architecture provides gas-transport pathways while serving as a stable scaffold for zeolite coating and subsequent catalyst loading.

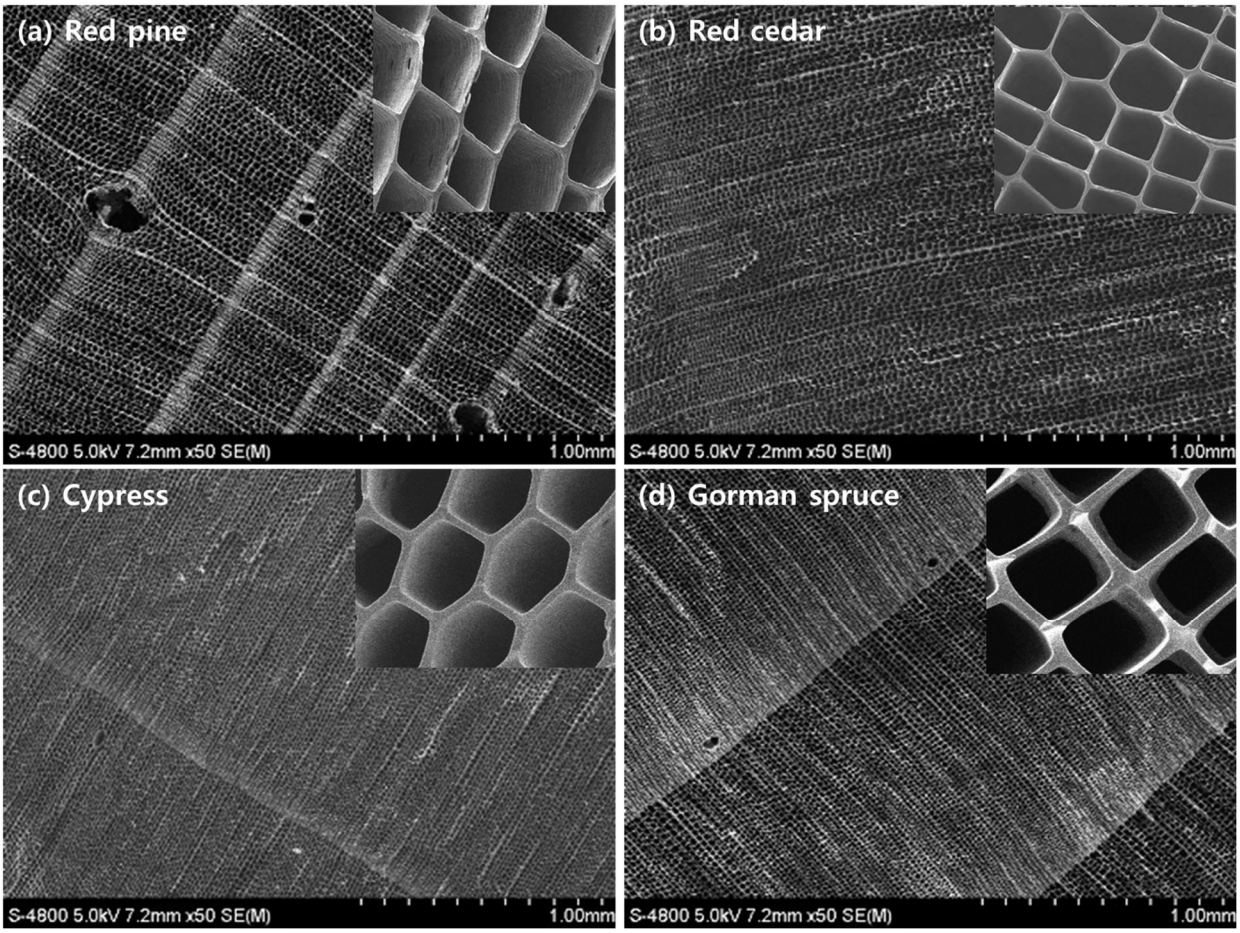


Figure 4. FESEM images of biomorphic carbon materials produced from (**a**) red pine, (**b**) red cedar, (**c**) cypress, and (**d**) Gorman spruce after carbonization, showing the preservation of the wood-derived cellular architecture and species-dependent pore morphology.

3.3. CNT Morphology and Support-Dependent Growth Behavior

TEM analysis confirmed the successful growth of multiwalled carbon nanotubes (MWCNTs) on all LTA-zeolite-coated biomorphic carbon monolith (BCM) supports (Figure 5). The CNTs exhibited well-defined tubular morphology with highly graphitized concentric walls, although their diameter and wall structure varied with the biomass-derived support. Red pine and red cedar produced CNTs with average diameters of approximately 30.6 nm and well-ordered graphitic layers, whereas cypress yielded smaller CNTs (~20.1 nm), indicating support-dependent variation in CNT diameter. Gorman spruce produced CNTs with an average diameter of ~30.1 nm and highly crystalline graphitic walls. HRTEM images revealed well-stacked graphene layers with interlayer spacings of approximately 0.296–0.34 nm, confirming good crystallinity. Overall, the TEM/HRTEM observations confirm the successful formation of MWCNTs on all LTA-zeolite-coated BCM supports and reveal clear support-dependent differences in CNT diameter and graphitic wall structure. These variations are discussed in relation to the distinct biomorphic architectures of the wood-derived supports.

3.4. Raman Analysis and TGA-Derived Carbon Deposition

According to our previous study, the Raman spectra of the synthesized CNT composites exhibited characteristic D and G bands near 1340 and 1600 cm^{-1}, respectively (Table 1) [14]. The D band is associated with structural defects and disorder, whereas the G band represents the in-plane vibration of sp^2-bonded graphitic carbon. The I_D/I_G ratio, commonly used

to evaluate graphitization and defect density, ranged from 0.80 to 1.00, consistent with CVD-grown MWCNTs [17–19]. These I_D/I_G values reflect differences in the relative degree of graphitic ordering and defect density among the CNT-containing samples.

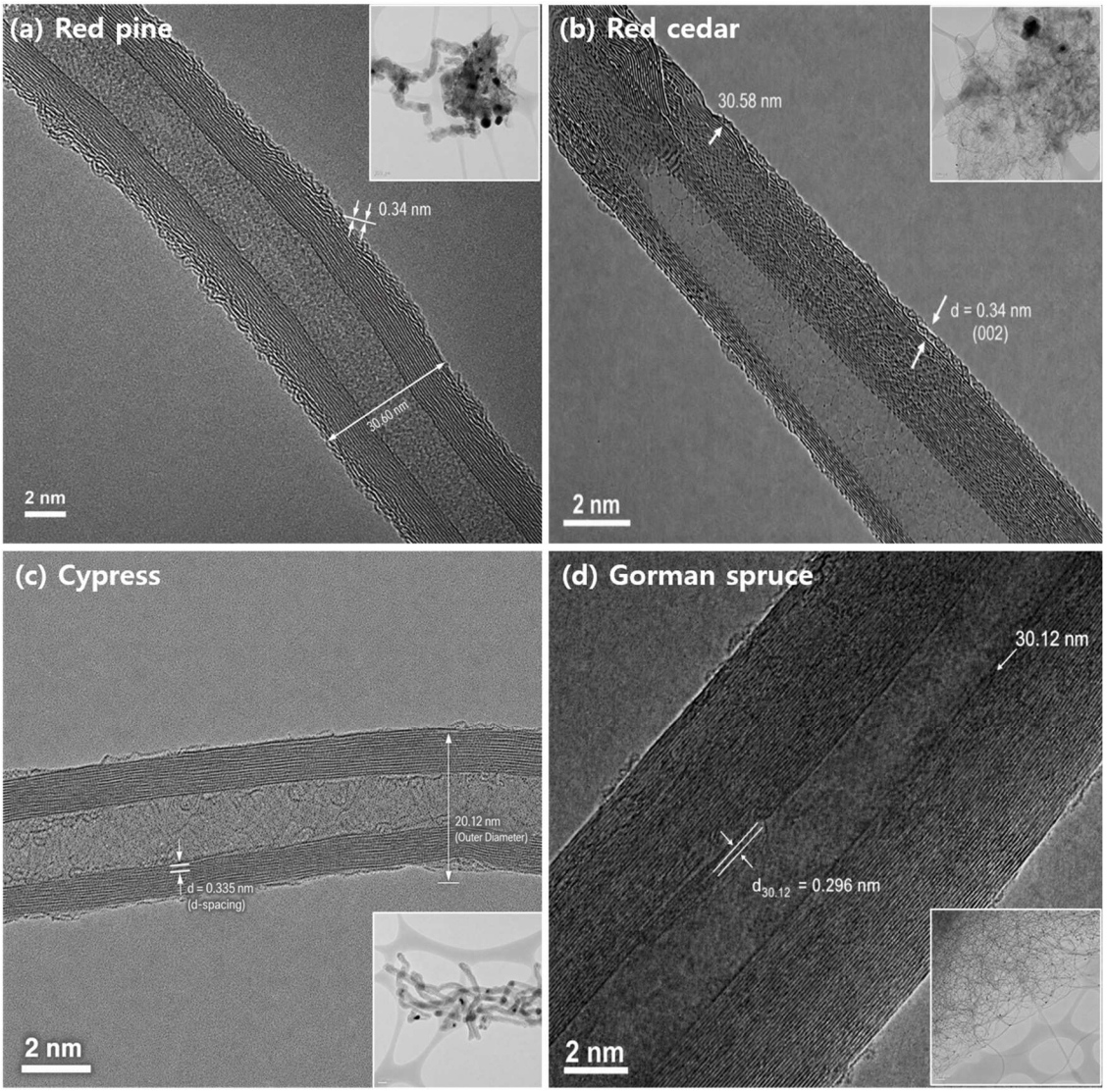


Figure 5. TEM and HRTEM images of CNTs synthesized on LTA-zeolite-coated BCMs at 650 °C for 60 min using (**a**) red pine, (**b**) red cedar, (**c**) cypress, and (**d**) Gorman spruce supports, showing well-developed MWCNTs with support-dependent diameters and highly ordered graphitic layers.

Table 1. Raman characteristics and TGA-derived carbon deposition of CNT-grown LTA-zeolite-coated BCMs.

Sample Name	Reaction Temperature [°C]	Raman Ratio [I_D/I_G]	TGA-Derived Carbon Deposition [%]
Red pine	650	1.00	2.40
Red cedar	650	1.00	2.21
Cypress	650	0.99	21.82
Gorman spruce	650	0.80	21.01

TGA-derived carbon deposition values were used for comparative assessment of the four CNT-grown BCM samples under identical nominal catalyst-loading and CCVD condi-

tions. Accordingly, these values are used for comparative assessment of carbon deposition among the four supports rather than as catalyst-normalized CNT yields. The TGA results were interpreted together with the TEM/HRTEM and Raman analyses because the deposited carbon may contain both MWCNTs and non-tubular carbon species formed during CCVD.

The TGA-derived carbon deposition values varied markedly among the four wood-derived supports, ranging from 2.21% to 21.82% (Table 1). Red pine and red cedar exhibited lower carbon deposition values of 2.40% and 2.21%, respectively, whereas cypress and Gorman spruce showed higher values of 21.82% and 21.01%, respectively. Among the investigated supports, the cypress-derived BCM exhibited the highest TGA-derived carbon deposition value. These differences indicate support-dependent variation in carbon deposition during CCVD. The observed trend is consistent with differences in biomorphic pore architecture and associated gas-transport characteristics, which may influence acetylene accessibility to catalyst-containing regions. Collectively, these analyses reveal support-dependent differences in carbon deposition and graphitic structural characteristics.

3.5. Porosity, Permeability, and Transport Characteristics

Figure 6 summarizes the porosity and mechanical properties of the four wood-derived BCM supports investigated in this study. As shown in Figure 6a, red pine and cypress exhibited the highest open and total porosities (≈87–90% and ≈83–85%, respectively), indicating highly interconnected porous structures favorable for gas transport. Red cedar and Gorman spruce showed comparatively lower porosities (~75–82%). Red cedar and Gorman spruce showed moderate porosity (≈75–82%). Despite the general inverse relationship between porosity and strength, species-dependent differences were evident (Figure 6b). Cypress exhibited the highest compressive strength among the four investigated supports (52.65 MPa), followed by red pine (36.78 MPa) and Gorman spruce (29.19 MPa), whereas red cedar exhibited the lowest compressive strength (23.76 MPa). As shown in Figure 6c,d, pore size alone did not determine strength. The mechanical performance appears to reflect the combined effects of wall thickness, pore morphology, and overall cellular architecture rather than pore size alone. Cypress, which exhibited the greatest wall thickness among the investigated supports, also showed the highest compressive strength. These results demonstrate that the anatomical structure of the biomass plays a critical role in determining the mechanical stability of the biomorphic carbon supports.

These findings indicate that cell-wall thickness contributes significantly to the mechanical stability of the porous carbon framework. Overall, differences in porosity, pore size, and wall thickness among the wood-derived supports are expected to influence gas transport (Table 2). High open porosity enhances precursor accessibility, while sufficient wall thickness and structural integrity preserve the biomorphic architecture during catalyst loading and CNT growth.

Therefore, the structural characteristics provide an important basis for interpreting the permeability behavior and the support-dependent differences in CNT growth observed in this study.

3.6. Permeability and Transport Characteristics

Permeability (κ) measurements revealed marked differences in gas transport behavior among the wood-derived BCM supports (Figure 7). Red pine exhibited the lowest permeability ($\kappa = 1.998 \times 10^{-8}$ m^2), indicating a relatively dense and less interconnected pore structure. Red cedar showed a slightly higher permeability ($\kappa = 7.113 \times 10^{-8}$ m^2), whereas Gorman spruce exhibited a substantially higher value ($\kappa = 1.092 \times 10^{-6}$ m^2). The highest permeability ($\kappa = 1.519 \times 10^{-6}$ m^2) was observed for cypress, indicating a highly open

and interconnected pore network. These permeability differences are consistent with the FESEM observations of the biomorphic structures. Supports possessing more open and continuous pore channels are expected to permit more efficient transport of acetylene to the catalyst sites during CCVD. Improved reactant accessibility can enhance carbon supply to catalyst-containing regions and reduce diffusion limitations within the interior of the structured support. Consequently, variations in pore architecture and permeability are likely to contribute to the differences in CNT growth behavior and carbon deposition among the samples.

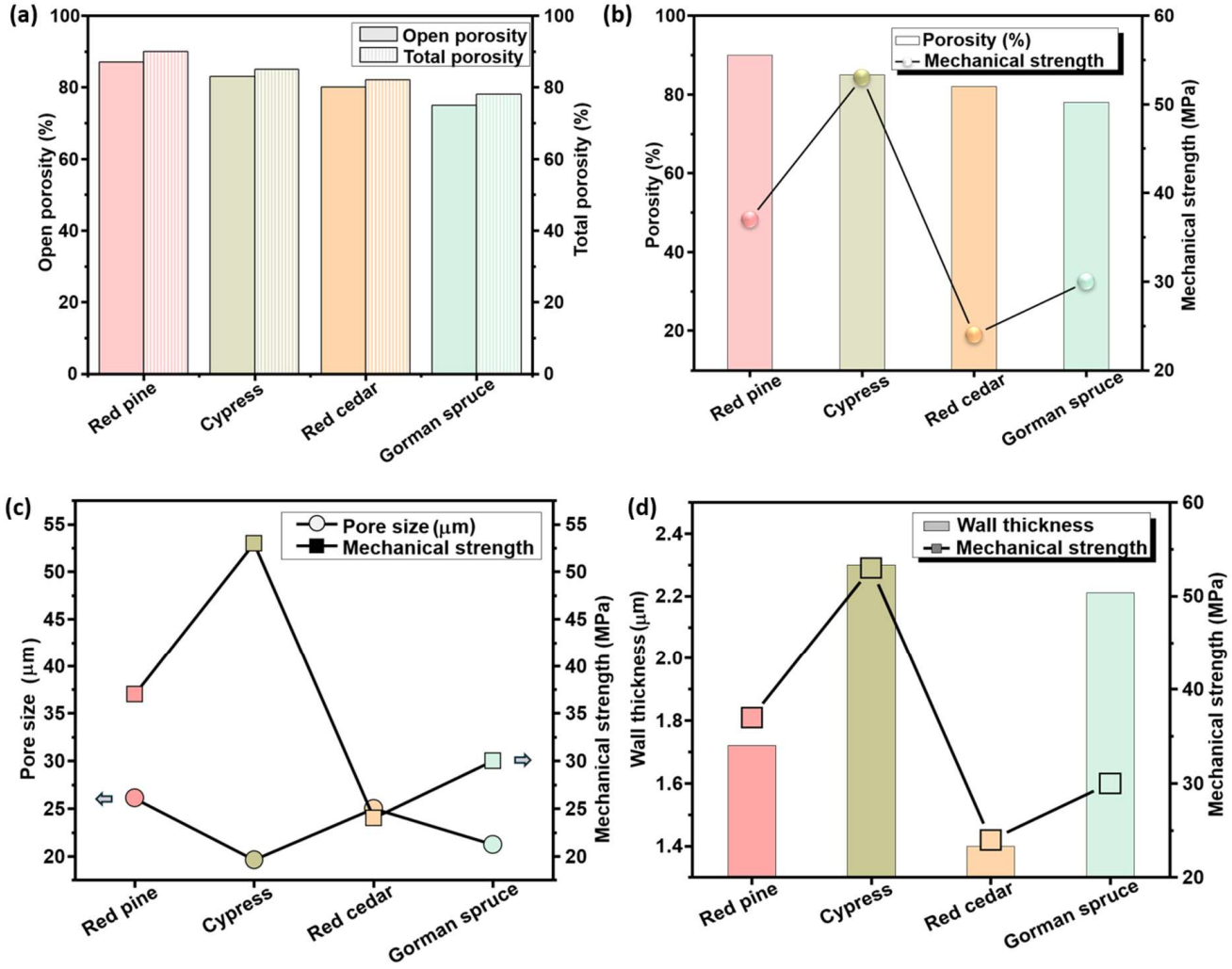


Figure 6. Comparative structural and mechanical properties of the four wood-derived BCM supports investigated in this study: (**a**) open and total porosity, (**b**) porosity–strength relationship, (**c**) pore size and strength, and (**d**) wall thickness and strength.

Table 2. Physical Properties and Morphologies of Biomorphic Carbon Materials.

Sample Name	Compressive Strength [MPa]	Pore Size and Porosity [μm]/[%]	Wall Thickness [μm]	Pore Morphology
Red pine	36.78	26.10/90	1.72	Square
Cypress	52.65	19.60/85	2.30	Hexagonal
Red cedar	23.76	25.00/82	1.40	Hexagonal
Gorman spruce	29.19	21.20/78	2.21	Square

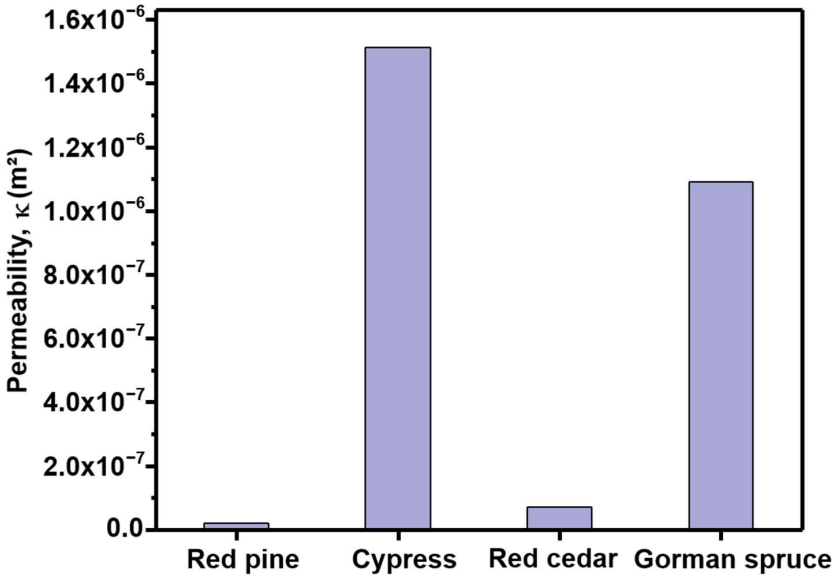


Figure 7. Permeability (κ, m^2) of the four wood-derived BCM supports, showing a trend from low permeability in red pine to high permeability in cypress.

4. Conclusions

LTA-zeolite-coated biomorphic carbon materials were successfully prepared from natural wood-derived carbon supports and used as structured substrates for cobalt-catalyzed CNT synthesis by CCVD. The carbonization process preserved the intrinsic cellular architecture of the wood precursors, producing interconnected biomorphic pore networks that served as hierarchical transport pathways. Among the four wood-derived supports, cypress exhibited the highest compressive strength (52.65 MPa), followed by red pine (36.78 MPa) and Gorman spruce (29.19 MPa), whereas red cedar showed the lowest compressive strength (23.76 MPa). The LTA-zeolite-coated BCMs provided a common catalyst-support platform for CNT synthesis across the four wood-derived structures. Multiwalled CNTs were successfully synthesized on all investigated supports, with support-dependent differences in CNT diameter and graphitic wall structure. The carbon deposition values varied substantially among the wood-derived supports, ranging from 2.21% to 21.82%. Red pine and red cedar exhibited comparatively low carbon deposition values of 2.40% and 2.21%, respectively, whereas cypress and Gorman spruce showed considerably higher values of 21.82% and 21.01%, respectively. The highest carbon deposition value was obtained for the cypress-derived BCM. These results demonstrate a pronounced support-dependent variation in carbon deposition during CCVD and indicate that the biomorphic pore architecture and associated transport characteristics are important factors influencing carbon growth on the structured supports. Future work should focus on quantitative characterization of cobalt particle-size distributions, loading efficiency, and chemical state before and after CCVD, optimization of CCVD parameters, and application-oriented evaluation of the resulting CNT/BCM composites.

Author Contributions: Conceptualization, I.J.K.; methodology, I.J.K.; formal analysis, I.J.K.; data curation, I.J.K.; writing—original draft, K.N.F.; writing—review and editing, K.N.F., M.R.U.D.B., S.Y.K., I.S.H., Y.S.K., S.C.L. and I.J.K. All authors have read and agreed to the published version of the manuscript.

Funding: This research received no external funding.

Data Availability Statement: The data presented in this study are available on request from the corresponding author.

Acknowledgments: ChatGPT (OpenAI, GPT-5.6 Sol) was used solely for language editing and grammar correction during the preparation of this manuscript. The authors reviewed and verified all AI-assisted edits and take full responsibility for the final content of the manuscript.

Conflicts of Interest: Author Md Rokon Ud Dowla Biswas was employed by the company HanTech Co., Ltd., Research & Development Center, Anyang-si, Gyeonggi-do, Republic of Korea; Authors Se Young Kim and In Sub Han were employed by the Institute Korea Institute of Energy Research, High Temperature Electrolysis Lab., Yuseung-gu, Daejeon City, Republic of Korea; Authors Young Suk Kim, Sung Chil Lee and Ik Jin Kim were employed by the Institute German Mongolian Institute for Resources and Technology, Ulaanbaatar, Mongolia. The remaining authors declare that the research was conducted in the absence of any commercial or financial relationships that could be construed as a potential conflict of interest.

References

1. Akasaka, T.; Watari, F. Capture of bacteria by flexible carbon nanotubes. *Acta Biomater.* **2009**, *5*, 607–612. [CrossRef] [PubMed]
2. Li, Y.-H.; Wang, S.; Luan, Z.; Ding, J.; Xu, C.; Wu, D. Adsorption of cadmium(II) from aqueous solution by surface oxidized carbon nanotubes. *Carbon* **2003**, *41*, 1057–1062. [CrossRef]
3. Lu, C.; Liu, C. Removal of nickel (II) from aqueous solution by carbon nanotubes. *J. Chem. Technol. Biotechnol.* **2006**, *81*, 1932–1940. [CrossRef]
4. Di, Z.C.; Ding, J.; Peng, X.J.; Li, Y.H.; Luan, Z.K.; Liang, J. Chromium adsorption by aligned carbon nanotubes supported ceria nanoparticles. *Chemosphere* **2006**, *62*, 861–865. [CrossRef] [PubMed]
5. Jourdain, V.; Bichara, C. Current understanding of the growth of carbon nanotubes in catalytic chemical vapour deposition. *Carbon* **2013**, *58*, 2–39. [CrossRef]
6. Nessim, G.D. Properties, synthesis, and growth mechanisms of carbon nanotubes with special focus on thermal chemical vapor deposition. *Nanoscale* **2010**, *2*, 1306–1323. [CrossRef] [PubMed]
7. Rashid, M.; Ralph, S.F. Carbon nanotube membranes: Synthesis, properties, and future filtration applications. *Nanomaterials* **2017**, *7*, 99. [CrossRef] [PubMed]
8. Cheung, C.L.; Kurtz, A.; Park, H.; Lieber, C.M. Diameter-controlled synthesis of carbon nanotubes. *J. Phys. Chem. B* **2002**, *106*, 2429–2433. [CrossRef]
9. Kitiyanan, B.; Alvarez, W.E.; Harwell, J.H.; Resasco, D.E. Controlled production of single-wall carbon nanotubes by catalytic decomposition of CO on bimetallic Co–Mo catalysts. *Chem. Phys. Lett.* **2000**, *317*, 497–503. [CrossRef]
10. Kumar, M.; Ando, Y. Controlling the diameter distribution of carbon nanotubes grown from camphor on a zeolite support. *Carbon* **2005**, *43*, 533–540. [CrossRef]
11. Pattinson, S.W.; Windle, A.H.; Koziol, K.K.K. Facile processing of zeolite based catalyst support for carbon nanotube synthesis. *Mater. Lett.* **2013**, *93*, 404–407. [CrossRef]
12. Lim, X.X.; Low, S.C.; Oh, W.D. A critical review of heterogeneous catalyst design for carbon nanotubes synthesis: Functionalities, performances, and prospects. *Fuel Process. Technol.* **2023**, *241*, 107624. [CrossRef]
13. Chen, Z.; Zhang, L.; Tang, Y.; Jia, Z. Adsorption of nicotine and tar from the mainstream smoke of cigarettes by oxidized carbon nanotubes. *Appl. Surf. Sci.* **2006**, *252*, 2933–2937. [CrossRef]
14. Park, J.G.; Basnet, B.; Kim, S.Y.; Kim, S.Y.; Kim, I.J. Harmonized processing of biomorphic materials for the synthesis of carbon nanotubes. *J. Ceram. Process. Res.* **2017**, *18*, 575–579.
15. Kim, Y.M.; Kim, I.J. Synthesis and Morphological Transformation of NaA Zeolite Crystals at High Temperature. *J. Korean Ceram. Soc.* **2006**, *43*, 1–3. [CrossRef]
16. Park, J.G.; Suh, M.J.; Kim, I.J. Heavy metal removal using carbon nanotube-biomorphic filters. *J. Ceram. Process. Res.* **2022**, *23*, 559–565.
17. Pawlyta, M.; Rouzaud, J.N.; Duber, S. Raman microspectroscopy characterization of carbon blacks: Spectral analysis and structural information. *Carbon* **2015**, *84*, 479–490. [CrossRef]
18. Pithaksinsakul, K.; Chaipornchalerm, P.; Bureekaew, S.; Wattanakit, C. 1D and 3D Carbon Nanomaterials Derived from Zeolite-Based Catalysts: Synthesis and Applications. *Small Struct.* **2026**, *7*, e202500596. [CrossRef]
19. Lehman, J.H.; Terrones, M.; Mansfield, E.; Hurst, K.E.; Meunier, V. Evaluating the characteristics of multiwall carbon nanotubes. *Carbon* **2011**, *49*, 2581–2602. [CrossRef]

Disclaimer/Publisher's Note: The statements, opinions and data contained in all publications are solely those of the individual author(s) and contributor(s) and not of MDPI and/or the editor(s). MDPI and/or the editor(s) disclaim responsibility for any injury to people or property resulting from any ideas, methods, instructions or products referred to in the content.